THE JOURNAL OF BIOLOGICAL CHEMISTRY
Vol. 280, No. 12, Issue of March 25, pp. 11770–11780, 2005
Printed in U.S.A.

Solution Structure of Enzyme IIA^{Chitobiose} from the *N,N′*-Diacetylchitobiose Branch of the *Escherichia coli* Phosphotransferase System*

Received for publication, December 20, 2004, and in revised form, January 13, 2005
Published, JBC Papers in Press, January 14, 2005, DOI 10.1074/jbc.M414300200

Chun Tang‡, David C. Williams, Jr.‡, Rodolfo Ghirlando§, and G. Marius Clore‡¶

From the Laboratories of ‡Chemical Physics and §Molecular Biology, NIDDK, National Institutes of Health, Bethesda, Maryland 20892-0520

The solution structure of trimeric *Escherichia coli* enzyme IIA^{Chb} (34 kDa), a component of the *N,N′*-diacetylchitobiose/lactose branch of the phosphotransferase signal transduction system, has been determined by NMR spectroscopy. Backbone residual dipolar couplings were used to provide long range orientational restraints, and long range ($|i - j| \geq 5$ residues) nuclear Overhauser enhancement restraints were derived exclusively from samples in which at least one subunit was ^{15}N/^{13}C/^{2}H/(Val-Leu-Ile)-methyl-protonated. Each subunit consists of a three-helix bundle. Hydrophobic residues lining helix 3 of each subunit are largely responsible for the formation of a parallel coiled-coil trimer. The active site histidines (His-89 from each subunit) are located in three symmetrically placed deep crevices located at the interface of two adjacent subunits (A and C, C and B, and B and A). Partially shielded from bulk solvent, structural modeling suggests that phosphorylated His-89 is stabilized by electrostatic interactions with the side chains of His-93 from the same subunit and Gln-91 from the adjacent subunit. Comparison with the x-ray structure of *Lactobacillus lactis* IIA^{Lac} reveals some substantial structural differences, particularly in regard to helix 3, which exhibits a 40° kink in IIA^{Lac} *versus* a 7° bend in IIA^{Chb}. This is associated with the presence of an unusually large (230-Å^3) buried hydrophobic cavity at the trimer interface in IIA^{Lac} that is reduced to only 45 Å^3 in IIA^{Chb}.

The bacterial phosphotransferase system (PTS)[1] is a prototypical signal transduction network in which translocation of sugars across the cytoplasmic membrane is coupled to phosphorylation (1–4). There are four branches of the pathway corresponding to four classes of enzymes II, glucose, mannose, mannitol, and lactose/chitobiose, which bear no sequence similarity to one another and for the most part no structural similarity either (2–4). The initial steps of the PTS are common to all branches of the pathway and involve the transfer of a phosphoryl group from phosphoenolpyruvate to the histidine phosphocarrier protein, HPr, via the intermediary enzyme I. Subsequently the phosphoryl group is transferred to sugar-specific enzymes II. Each enzyme II consists of two cytoplasmic domains, IIA and IIB, and a transmembrane sugar permease IIC, which may or may not be covalently linked. IIA accepts the phosphoryl group from HPr and donates it to IIB; IIC catalyzes the transport of the sugar across the membrane and its phosphorylation by IIB. Structures of many of the individual cytoplasmic components of the PTS have been solved by either NMR (5–11) or crystallography (12–22), and more recently we have reported the solution NMR structures of a number of protein-protein complexes of the PTS (23–26). As part of our continuing structural work on the PTS, we present the solution structure of *Escherichia coli N,N′*-diacetylchitobiose-specific enzyme IIA (IIA^{Chb}) using multidimensional NMR spectroscopy.

The *E. coli N,N′*-diacetylchitobiose-specific enzymes II (II^{Chb}) are part of the lactose/chitobiose branch of the PTS (27). The A, B, and C components of II^{Chb} are encoded by a single operon and expressed as individual proteins (27). NMR (8, 9) and crystal structures of *E. coli* IIB^{Chb} have been solved and bear surprising similarity to the structure of IIB^{Mannitol} (11), as well as to that of the low molecular weight eukaryotic protein tyrosine phosphatases (28, 29), despite the absence of any significant sequence identity. No structure, however, has been determined as yet for *E. coli* IIA^{Chb}. The analogous system in *Lactobacillus* and *Staphylococcus* comprises the lactose-specific enzymes II (II^{Lac}) (30, 31). The crystal structure of IIA^{Lac} from *Lactobacillus lactis* has been solved and been shown to consist of a symmetric homotrimer (18): each subunit comprises three antiparallel helices; the trimer interface consists of a parallel coiled-coil formed by the C-terminal helix from each subunit; and the trimer interface is partially stabilized by a metal ion coordinated to the side chains of three buried, symmetry-related, aspartate residues, one from each subunit. The crystal structure of IIA^{Lac}, however, displays a highly unusual feature in the form of a very large (230-Å^3), completely buried cavity at the trimer interface that is associated with the presence of a $\sim$40° kink in helix 3 and accommodates the heavy atom derivative trimethyl lead acetate (18). *E. coli* IIA^{Chb} and *L. lactis* IIA^{Lac} share 35% sequence identity and 63% amino acid similarity with no gaps or insertions (Fig. 1). In addition,

---

* This work was supported in part by the AIDS Targeted Anti-Viral Program of the Office of the Director of the National Institutes of Health (to G. M. C.). The costs of publication of this article were defrayed in part by the payment of page charges. This article must therefore be hereby marked "*advertisement*" in accordance with 18 U.S.C. Section 1734 solely to indicate this fact.

The atomic coordinates and experimental NMR restraints (code 1WCR) have been deposited in the Protein Data Bank, Research Collaboratory for Structural Bioinformatics, Rutgers University, New Brunswick, NJ (http://www.rcsb.org/).

¶ To whom correspondence should be addressed: Laboratory of Chemical Physics, Bldg. 5, Rm. B1–30I, NIDDK, National Institutes of Health, Bethesda, MD 20892-0520. Tel.: 301-496-0782; Fax: 301-496-0825; E-mail: mariusc@intra.niddk.nih.gov.

[1] The abbreviations used are: PTS, phosphotransferase system; Chb, *N,N′*-diacetylchitobiose; HPr, histidine-containing phosphocarrier protein; IIA^{Chb}, IIB^{Chb}, and IIC^{Chb}, A, B, and C domains, respectively, of the *N,N′*-diacetylchitobiose transporter II^{Chb}; IIA$^{\text{Chb*}}$, double mutant of IIA^{Chb} comprising a 13-residue deletion at the N-terminus and an Asp to Leu mutation at position 92 (of the double mutant); NOE, nuclear Overhauser effect; HSQC, heteronuclear single quantum coherence; TROSY, transverse relaxation optimized spectroscopy; r.m.s., root mean square.

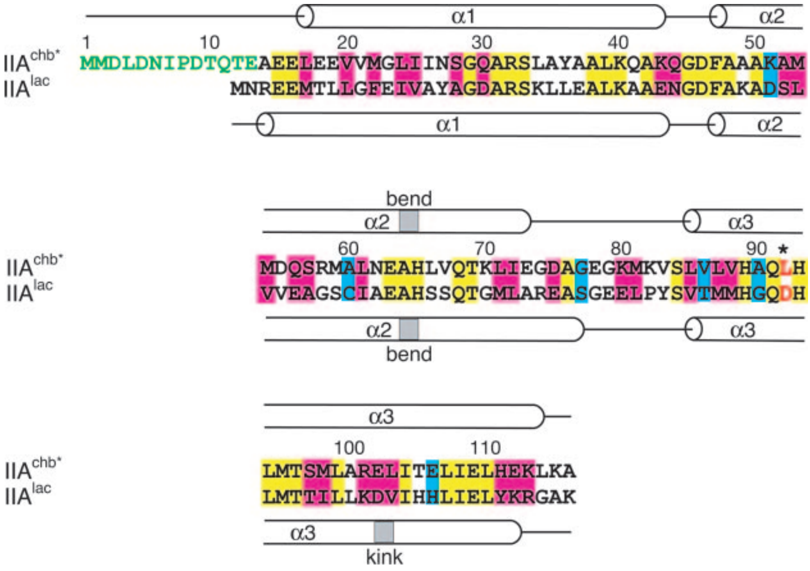
α1
α2
1
10
20
30
40
50
IIA^chb*^
IIA^lac^
MMDLDNIPDTQTEAEELEEVVMGLIINSGQARSLAYAALKQAKQGDFAAAKAM
MNREEMTLLGFEIVAYAGDARSKLLEALKAAENGDFAKADSL
α1
α2
bend
α2
α3
60
70
80
90
*
IIA^chb*^
IIA^lac^
MDQSRMALNEAHLVQTKLIEGDAGEGKMKVSLVLVHAQLH
VVEAGSCIAEAHSSQTGMLAREASGEELPYSVTMMHGQDH
α2
α3
bend
α3
100
110
IIA^chb*^
IIA^lac^
LMTSMLARELITELIELHEKLKA
LMTTILLKDVIHHLIELYKRGAK
α3
kink

FIG. 1. **Sequence alignment of *E. coli* IIA^{Chb} and *L. lactis* IIA^{Lac}.** The residue shown at position 92 of IIA^{Chb} is that of the IIA^{Chb}-NΔ13D92L double mutant (IIA^{Chb*}) used for structural studies; both wild-type IIA^{Chb} and *L. lactis* IIA^{Lac} have an Asp residue at this position. The N-terminal 13 residues that were deleted from wild-type IIA^{Chb} are colored in *green*; residue 92, the site of the engineered Asp to Leu mutation, is colored in *bold red*. Identical residues between IIA^{Chb} and IIA^{Lac} are shaded in *yellow*, closely similar ones are in *magenta*, and remotely similar ones are in *cyan*.

binding of divalent cations to *E. coli* IIA^{Chb} significantly enhances its thermostability relative to the apoform, increasing in the order Mg^{2+}, Cu^{2+}, and Ni^{2+} (33). It has also been reported, on the basis of analytical ultracentrifugation data, that *E. coli* IIA^{Chb} is dimeric in solution (34) in clear contrast to the trimeric state of IIA^{Lac} (18). Since the three symmetrically related active site histidines in IIA^{Lac} are located in a crevice formed by the interface of two adjacent subunits (18), this result would imply that the surface topology of the active sites and the spatial relationships of side chains within the active sites are very different in IIA^{Lac} and IIA^{Chb}. If true, this would be highly unexpected given the close sequence and functional relationship between IIA^{Lac} and IIA^{Chb}. Intrigued by this discrepancy, we initiated our own investigation of the oligomerization state and three-dimensional solution structure of *E. coli* IIA^{Chb}.

EXPERIMENTAL PROCEDURES

Protein Purification and Mutagenesis—The plasmid for wild-type *E. coli* IIA^{Chb} was a kind gift from Dr. Saul Roseman (The Johns Hopkins University, Baltimore, MD). The plasmid was propagated in TOP10 cells, and IIA^{Chb} was expressed in BL21-Star cells (Invitrogen) at 37 °C. After induction with isopropyl β-D-thiogalactopyranoside, cells were harvested and microfluidized in 10 mM Tris·HCl, pH 7.5, buffer. The protein was purified using a DEAE-Sepharose anion-exchange column followed by a preparative Superdex-75 size exclusion column (Amersham Biosciences). IIA^{Chb} was denatured with 6 M guanidine HCl solution (pretreated with Chelex; Bio-Rad) at pH 3 and incubated at 37 °C overnight to remove residual phosphoryl groups on the protein. The pH of the denatured protein solution was then raised by the addition of 1 M Tris·HCl buffer. The protein solution was then dialyzed against either 10 mM sodium phosphate buffer (pH 6.5) or 10 mM Tris·HCl buffer (pH 8) containing 100 μM divalent cation to remove guanidine HCl and refold the protein; seven metal ions, Mg^{2+}, Ca^{2+}, Mn^{2+}, Co^{2+}, Ni^{2+}, Cu^{2+}, and Zn^{2+}, were tested individually, yielding seven different samples. Excess metal ions in each metal-loaded protein sample were washed away by extensive buffer exchange in a concentrator, and the protein was further concentrated.

The N-terminal deletion mutation (IIA^{Chb}-NΔ13) in which the first 13 residues were removed and the subsequent point mutation, IIA^{Chb}-NΔ13/D92L, were introduced using the QuikChange mutagenesis kit (Stratagene, La Jolla, CA). The primers were designed according to the manufacturer's instructions. The sequences of the two mutants (IIA^{Chb}-NΔ13 and IIA^{Chb}-NΔ13/D92L) were confirmed by DNA sequencing (Davis Sequencing, Davis, CA). The two mutant proteins were purified using the same procedure described above for the wild-type protein. Typically 50 mg of protein were obtained from a 1-liter culture. The masses of the unlabeled proteins (wild type, NΔ13, and NΔ13/D92L) were confirmed by electrospray ionization mass spectrometry. The double mutant NΔ13/D92L is referred to hereafter as IIA^{Chb*}.

(Ile/Leu/Val)-methyl-protonated and otherwise fully deuterated IIA^{Chb}-NΔ13/D92L (abbreviated as ILV-IIA^{Chb*}) was expressed based on the protocol described previously (35). Briefly cells were grown in M9 minimal medium prepared in D_2O with [$^2H_7$,$^{13}C_6$]glucose and [^{15}N]NH_4Cl as the carbon and nitrogen sources, respectively. 80 mg of α-[$^{13}C_5$,3-$^2H_1$]ketoisovalerate and 50 mg of α-[$^{13}C_4$,3,3-$^2H_2$]ketobutyrate (Cambridge Isotopes, Andover, MA) were added into 1 liter of culture 45 min prior to induction at an $A_{600\ nm}$ of ~0.6. After induction with isopropyl β-D-thiogalactopyranoside, cells were grown under vigorous shaking for another 4 h before harvesting. Purified in H_2O buffer, the protein sample carries protons only at backbone and side-chain amides, γ-methyls of Val residues, and δ-methyl(s) of Ile/Leu residues.

Light Scattering—Static light-scattering data were collected using analytical size exclusion chromatography on a Superdex-75 column (Amersham Biosciences) in tandem with DAWN EOS light scattering and refractive index detectors (Wyatt Technology, Santa Barbara, CA). 100 μl of 75 μg of protein was applied to the pre-equilibrated Superdex-75 column at a flow rate of 0.5 ml/min at room temperature (20 °C). The running buffer consisted of either 10 mM sodium phosphate buffer, pH 6.5, or 10 mM Tris·HCl buffer, pH 7.5, containing 0.02% NaN_3, 1 mM methionine, and 300 mM NaCl. The protein elution profile was monitored by the refractive index detector, and light-scattering measurements were made every 4 μl for a total elution volume of 20 ml. The data were analyzed using the manufacturer's proprietary software.

The translational diffusion coefficient of the IIA^{Chb}-NΔ13/D92L double mutant (IIA^{Chb*}) was determined from autocorrelation analysis of quasielastically scattered light. Autocorrelation functions were collected on a BI-9000 AT autocorrelator (Brookhaven Instruments, Long Island, NY) at an angle of 90° with sampling times ranging from 0.5 μs to 10 ms. The diffusion coefficient, $D_{20,w}$, was derived from autocorrelation functions of 10 independent measurements using the software provided by Brookhaven Instruments. The corresponding Stokes radius, R_s, was calculated using the equation $R_s = kT/6\pi\eta D_{20,w}$ where η represents the solvent viscosity, T is the absolute temperature, and k is the Boltzmann constant. The predicted translational diffusion coefficient and Stokes radius for the crystal structure of *L. lactis* IIA^{Lac} (18) were calculated using the program HYDROPRO (36).

NMR Data Collection and Analysis—All NMR samples were prepared in 10 mM sodium phosphate buffer, pH 6.5, containing 0.02% NaN_3 and 1 mM methionine. NMR spectra were collected at 30 °C on Bruker DMX500, DMX600, DRX600, DMX750, and DRX800 spectrometers equipped either with x,y,z-shielded gradient triple resonance probes or z-shielded gradient triple resonance cryoprobes. Spectra were processed with the NMRPipe/nmrDraw suite (37) and analyzed using the PIPP/CAPP/STAPP package (38). Sequential resonance assignments were derived from analysis of transverse relaxation optimized (TROSY)-based triple resonance three-dimensional NMR experiments (39–42), including HNCO, HN(CO)CA, HNCA, HNCB, and HN(CO)CB recorded on the ILV-IIA^{Chb*} sample. Nearly complete side-chain assignments were obtained from analysis of a three-dimensional HCCH-TOCSY experiment recorded on a ^{13}C,^{15}N-labeled IIA^{Chb*} sample. A triple resonance CBCA(CO)NH was also recorded on the ^{13}C,^{15}N-labeled IIA^{Chb*} sample to obtain $^{13}C\alpha$/$^{13}C\beta$ chemical shifts free of the offsets resulting from perdeuteration.

Backbone ϕ/ψ torsion angle restraints were derived from backbone ^{1}H, ^{15}N, and ^{13}C chemical shifts using the program TALOS (43). Side-chain torsion angle restraints were derived from $^3J_{NC\gamma}$, $^3J_{C'C\gamma}$, and $^3J_{C\alpha C}\delta$ coupling constants measured using quantitative J correlation experiments (44).

Intersubunit nuclear Overhauser enhancements (NOEs) were obtained from a three-dimensional ^{13}C-separated/^{12}C-filtered NOE spectrum collected on a sample comprising a 1:1 mixture of unlabeled IIA^{Chb*} and labeled ILV-IIA^{Chb*} (42). To ensure complete mixing of the subunits, the 1:1 mixture of the labeled and unlabeled proteins was denatured in 6 M guanidine HCl and then refolded into the NMR buffer (10 mM sodium phosphate buffer, pH 6.5, 0.02% NaN$_3$, and 1 mM methionine). Intramolecular long range NOEs were obtained from four-dimensional ^{13}C/^{15}N-separated and ^{13}C/^{13}C-separated NOE spectra collected on the ILV-IIA^{Chb*} sample. As methyl-methyl NOE interactions in the unfiltered NOE spectra contain both intra- and intermolecular information, care was taken to ensure that assigned intramolecular NOE cross-peaks did not appear in the three-dimensional ^{13}C-separated/^{12}C-filtered NOE spectrum. NOEs involving backbone amide protons were obtained from a three-dimensional ^{15}N-separated NOE spectrum.

Backbone $^1D_{NH}$, $^1D_{NC'}$, and $^1D_{C\alpha C'}$ residual dipolar couplings were obtained from the difference between the ^1J scalar couplings measured in dilute liquid crystalline (15 mg/ml phage pf1 (45, 46)) and isotropic (water) media. $^1J_{NH}$ and $^1J_{NC'}$ couplings were measured from the splittings in three-dimensional HNCO-TROSY-based experiments (47), and $^1J_{C\alpha C'}$ couplings were derived from an intensity-modulated HN(CO)CA-TROSY experiment (48).

Structure Calculation—NOE-derived interproton distance restraints were classified into distance ranges of 1.8–2.7, 1.8–3.3, 1.8–5.0, and 1.8–6 Å, corresponding to strong, medium, weak, and very weak NOE cross-peak intensities, respectively. An additional 0.5 Å was added to the upper distance bound of distance restraints involving methyl groups (0.5 Å per methyl group), and 0.2 Å was added to the upper bounds for strong and medium NOE restraints involving amide protons. Non-stereospecifically assigned methyl protons and ambiguous intermolecular NOEs were represented by a $(\Sigma r^{-6})^{-1/6}$ sum. The error ranges used for the torsion angle restraints (which are represented by square-well potentials) are ±20° for the backbone ϕ/ψ angles within helical regions and ±20° for χ_1 and ±30° for χ_2 side-chain torsion angles. χ_1 restraints for aliphatic side chains that are not in the t rotamer and not experiencing rotamer averaging ($^3J_{C\gamma N} < 1.0$ Hz) were set to $0 \pm 80°$.

Structures were calculated using a well established protocol (49–52) from the experimental NMR restraints by simulated annealing in torsion angle space (53) using the program Xplor-NIH (54). The coordinates of the three subunits were restrained to their average positions (after best fitting) by a non-crystallographic symmetry restraint. The non-bonded contacts in the target function were represented by a quartic van der Waals repulsion term (49) supplemented by multidimensional torsion angle (55) and backbone hydrogen bonding (56) data base potentials of mean force. A radius of gyration restraint was used to ensure optimal packing (57). Structure figures were generated with the programs VMD-XPLOR (58) and Pymol (59). Reweighted atomic density probability maps were calculated from the structure ensemble as described previously (60). Modeling of the phosphorylated state was carried out by manually docking a phosphoryl group in the vicinity of the Nϵ-1 atom of the active site His-89 of the restrained regularized mean structure in VMD-XPLOR followed by regularization using Xplor-NIH, keeping all coordinates fixed with the exception of the side chain of His-89 and the phosphoryl group.

RESULTS AND DISCUSSION

Engineering a Monodisperse Trimer—^{1}H-^{15}N heteronuclear single quantum coherence (HSQC) correlation spectra of ^{15}N-labeled IIA^{Chb} in both the apoform and loaded with diverse divalent cations, including Mg^{2+}, Ca^{2+}, Mn^{2+}, Co^{2+}, Ni^{2+}, Cu^{2+}, and Zn^{2+}, are all broad and poorly dispersed, indicative of chemical exchange between various states. Of these various samples, Ni^{2+}-charged IIA^{Chb} displayed the best spectrum (Fig. 2*A*), suggesting slightly more favorable exchange dynamics, consistent with the prior observation that Ni^{2+} has the largest effect in enhancing the thermostability of IIA^{Chb} (33).

Ni^{2+}-charged IIA^{Chb} was then subjected to light-scattering analysis. The intensity of light scattered by a molecule is directly proportional to molar mass; thus static light scattering used in tandem with analytical size exclusion chromatography can measure the average molecular weight of the eluted fractions on the fly. Light-scattering analysis reveals that wild-type Ni^{2+}-IIA^{Chb} is a mixture of many species of different molecular masses ranging from 35 to 70 kDa, and there is no predominant species of defined molecular weight in the mixture (Fig. 3*A*, *blue symbols*). This result fully accounts for the poor quality of the ^{1}H-^{15}N correlation spectrum of Ni^{2+}-IIA^{Chb} (Fig. 2*A*). Significantly, even at the leading edge of the gel filtration peak where the protein concentration is only ~140

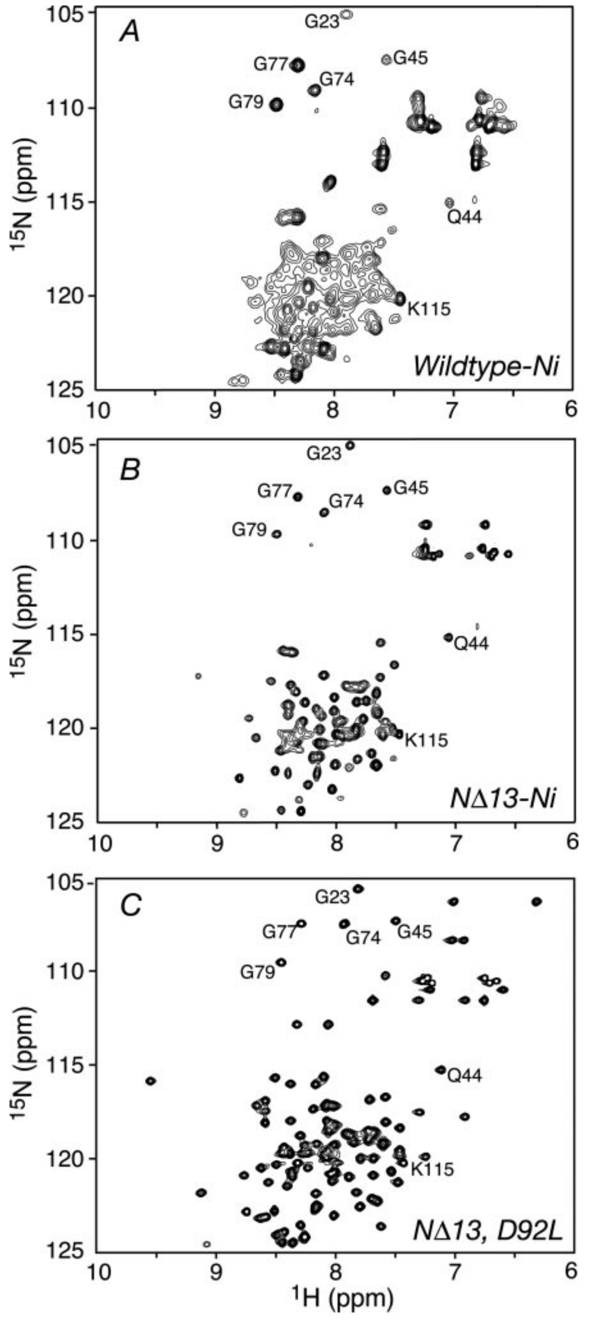

FIG. 2. **NMR spectral characterization of IIA^{Chb} wild-type and mutant proteins.** ^{1}H-^{15}N HSQC spectra of ^{15}N-labeled wild-type IIA^{Chb} loaded with Ni^{2+} (*A*), the ^{15}N-labeled IIA^{Chb}-NΔ13 deletion mutant loaded with Ni^{2+} (*B*), and the ^{15}N-labeled IIA^{Chb}-NΔ13/D92L double mutant (IIA^{Chb*}) (*C*). Outlying cross-peaks in the spectrum shown in *A* that match closely to those in *C* are tentatively assigned in *A* and *B* and are labeled in all three spectra. In addition, the cross-peak position for the C-terminal residue, Ala-116, is essentially identical for all three constructs and is located at 130.9 ppm in the ^{15}N dimension (not shown).

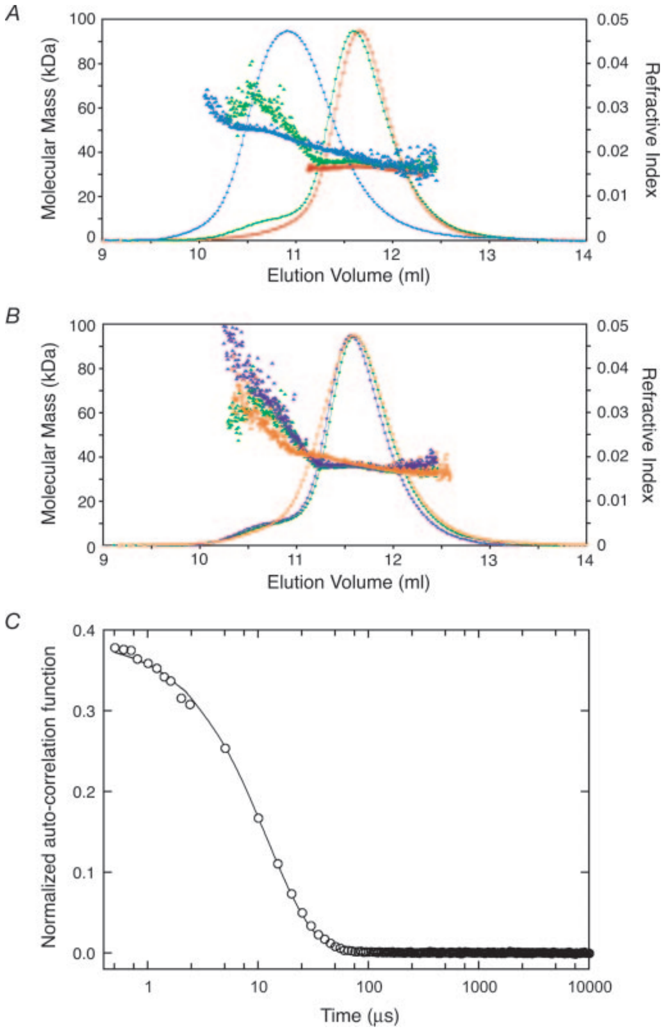

FIG. 3. **Static and dynamic light scattering of IIA^{Chb} wild-type and mutant proteins.** *A* and *B*, size exclusion column elution profiles of IIA^{Chb} proteins characterized by steady state light scattering and refractive index. The magnitude of the refractive index is proportional to the total protein concentration (represented by *filled circles* and *lines*); a value of 0.01 for the refractive index is equivalent to $\sim$0.012 mg/ml protein. The average molecular masses of the eluted fractions determined by static light scattering are represented by *filled triangles*. Unless otherwise noted, all the samples were prepared in 10 mM sodium phosphate buffer, pH 6.5, containing 300 mM NaCl, 1 mM methionine, and 0.02% NaN$_3$. The sequence-dependent molecular mass composition of wild-type and variant IIA^{Chb} proteins is analyzed in *A*. The data for wild-type IIA^{Chb} loaded with Ni^{2+}, the IIA^{Chb}-NΔ13 deletion mutant loaded with Ni^{2+}, and the IIA^{Chb}-NΔ13/D92L double mutant (IIA^{Chb*}) are displayed in *blue*, *green* and *red*, respectively. The IIA^{Chb}-NΔ13/D92L double mutant (IIA^{Chb*}) behaves as a homogeneous, monodisperse trimer. Note that additional data points are plotted for the wild-type IIA^{Chb} light-scattering data before the signal is completely buried in the noise. The influence of buffer composition on the molecular weight composition of the IIA^{Chb}-NΔ13 deletion mutant is shown in *B*. Data for the Ni^{2+}-loaded protein in phosphate buffer (same as in *A* for comparison) and in Tris buffer (10 mM Tris·HCl, pH 7.5, 300 mM NaCl, 1 mM methionine, and 0.02% NaN$_3$) are shown in *green* and *purple*, respectively; data for the apoprotein (sample stripped of Ni^{2+}) in phosphate buffer is shown in *orange*. *C*, dynamic light-scattering measurements performed on the IIA^{Chb}-NΔ13/D92L double mutant (IIA^{Chb*}). The average values of the normalized autocorrelation function obtained from 10 individual experiments, corresponding to a total collection time of 12 min, are shown as *open circles*, and the best second cumulant fit is shown as a *solid line* through the experimental data points.

nM, the molecular mass never falls below 3 times the monomer molecular mass (12,747.7 Da), which is the molecular mass of a trimer. Further, as increasing concentration promotes higher order oligomerization, our light-scattering results are not consistent with the previous report that IIA^{Chb} behaves as a dimer even at a concentration of 30 μM or an optical density of 1 at 230 nm (34).

To obtain a homogeneous and monodisperse sample suitable for structural studies, we constructed a series of IIA^{Chb} variants using rational mutagenesis. We first noted that (*a*) the N-terminal 11 residues of IIA^{Chb} are not present in *L. lactis* IIA^{Lac} (Fig. 1), (*b*) the N-terminal two residues of IIA^{Lac} have high *B*-factors in the crystal structure (18), and (*c*) the secondary structure of the first 13 residues of IIA^{Chb} is predicted to be unstructured (PredictProtein, cubic.bioc.columbia.edu/predictprotein/). On this basis we constructed a deletion mutant of IIA^{Chb} lacking the N-terminal 13 residues, IIA^{Chb}-NΔ13 (Fig. 1). The light-scattering profile for Ni^{2+}-loaded IIA^{Chb}-NΔ13 is also a mixture of different molecular mass species ranging from 35 to 70 kDa (Fig. 3*A*, *green symbols*). Unlike full-length IIA^{Chb}, however, the IIA^{Chb}-NΔ13 sample contains a major species with a molecular mass of $\sim$35 kDa, 3 times the monomer molecular mass. Thus, IIA^{Chb}-NΔ13 is a mixture comprising a predominant trimeric species in conjunction with high molecular weight aggregates. Judging from the gel filtration profile quantified by refractive index, the trimeric species makes up over 90% of the total protein. The trimer is in equilibrium with the high molecular weight aggregates as a sample drawn from the trimer peak yields an identical elution profile when loaded again on the gel filtration column. Consistent with the light-scattering analysis, the ^{1}H-^{15}N HSQC spectrum of ^{15}N-labeled IIA^{Chb}-NΔ13 in the presence of Ni^{2+} displays far better resolved peaks than that of the wild-type protein (Fig. 2*B*).

In addition to improving the thermostability of IIA^{Chb}-NΔ13, the presence of Ni^{2+} paradoxically promotes protein aggregation. Ni^{2+}-charged IIA^{Chb}-NΔ13 prepared in Tris buffer (Fig. 3*B*, *blue*) yields a similar light-scattering profile to that prepared in phosphate buffer (Fig. 3*B*, *green*) characterized by a major species of $\sim$35 kDa. However, the molecular mass of the high order aggregates in Tris buffer extends beyond 100 kDa, indicative of more extensive aggregation. The difference is likely due to the weak metal cation affinity of phosphate that scavenges Ni^{2+} from solution and reduces metal-induced nonspecific aggregation. In contrast, metal-stripped IIA^{Chb}-NΔ13 contains no predominant species of defined molecular weight (Fig. 3*B*, *orange symbols*). This observation confirms the importance of metal cations in stabilizing the trimer interface, presumably in the same fashion as that observed in the crystal structure of *L. lactis* IIA^{Lac} where a metal ion is coordinated by three symmetry-related buried aspartate side chains, one from each subunit (18). As such, the role of divalent metal cations is double edged: they promote trimer formation but simultaneously induce a small degree of nonspecific protein aggregation.

To circumvent the dual behavior of metal cations, we introduced an Asp to Leu mutation in IIA^{Chb}-NΔ13 at the site (residue 92) corresponding to the buried aspartate involved in metal ion coordination in IIA^{Lac}. Since Leu and Asp have similarly branched side chains, the Asp → Leu mutation should eliminate the need for a metal cation at the trimer interface by substituting hydrophobic methyl-methyl interactions in place of the metal cation. To test this hypothesis, we conducted light-scattering measurements on the IIA^{Chb}-NΔ13/D92L double mutant (IIA^{Chb*}). The light-scattering profile shows a single species at 33.5 kDa (Fig. 3*A*, *red symbols*) in excellent agreement with the calculated molecular mass of 33.7 kDa for a IIA^{Chb*} trimer (11,241.1 Da per subunit). Unlike the IIA^{Chb}-NΔ13 deletion mutant, the choice of buffer (phosphate *versus* Tris) does not have any impact on the molecular weight of the sample (data not shown). To further corroborate these results, dynamic light scattering on IIA^{Chb*} was also carried out, and a single exponential autocorrelation profile was obtained that fits to a single species with a diffusion coefficient $D_{20,w}$ of 8.1 ± 0.2 × 10^{-7} cm^2·s^{-1} and a Stokes radius of 26.5 ± 0.6 Å (Fig. 3*C*). These measured values are in very close agreement with those calculated (36) from the crystal structure (18) of trimeric IIA^{Lac} (8.28 × 10^{-7} cm^2·s^{-1} and 25.9 Å, respectively).

Consistent with the light-scattering results, ^{15}N-labeled IIA^{Chb*} displays a relatively well resolved ^{1}H-^{15}N HSQC spectrum: the peaks have reasonable linewidths for a ~34-kDa protein, and the number of cross-peaks is close to that expected for a symmetric trimer of 103 residues per subunit (Fig. 2*C*). Moreover some of the outlying cross-peaks in the ^{1}H-^{15}N HSQC spectrum of wild-type IIA^{Chb} (Fig. 2*A*) match closely to those of IIA^{Chb}-NΔ13 (Fig. 2*B*) and IIA^{Chb*} (Fig. 2*C*), demonstrating that the structures remain largely intact despite the mutations introduced. In addition, titration of unlabeled HPr results in a systematic perturbation in the chemical shifts for a subset of cross-peaks in the ^{1}H-^{15}N HSQC spectrum of IIA^{Chb*} (data not shown), indicative of a specific interaction between HPr and IIA^{Chb*}. Finally ^{1}H-^{15}N correlation spectroscopy and mass spectrometry indicate that IIA^{Chb*} is readily phosphorylated upon incubation with phosphoenolpyruvate and catalytic amounts of enzyme I and HPr (data not shown), indicating the functional relevance of IIA^{Chb*}. Hence the current experimental data lead one to a single conclusion: wild-type IIA^{Chb} is a mixture of aggregates of different molecular weight species, whereas the double mutant IIA^{Chb*}, containing both the N-terminal deletion and the Asp → Leu point mutation, yields a homogenous, monodisperse trimeric form suitable for structural studies. The discrepancy with previous work in which it was proposed that wild-type II^{Chb} is a dimer on the basis of analytical ultracentrifugation studies (34) may possibly be due to the unusually high centrifugation speeds (>35,000 rpm) used (www.beckman.com/resourcecenter/labresour-ces/sia/pdf/rotor_speed_equilibrium.pdf).

Methyl-based NOEs for Structure Determination—On the basis of the above results, all structural NMR work was carried out on the IIA^{Chb}-NΔ13/D92L double mutant IIA^{Chb*}. Many of the NMR experiments were carried out on a ^{2}H/^{15}N/^{13}C/(Ile-Leu-Val)-methyl-protonated sample, denoted as ILV-IIA^{Chb*}. Perdeuteration lowers the proton density and slows the overall transverse relaxation rates for larger proteins, while fast rotation and 3-fold degeneracy give methyl protons a further edge in relaxation properties (35). Moreover, as hydrophobic side chains are often involved in protein tertiary folding, retaining methyl protons still yields a large number of long range interresidue NOEs ($|i - j| > 5$) in a large system. The necessity of such a labeling strategy was dictated by the fact the ~34-kDa IIA^{Chb*} trimer is essentially all helical with the long axes of the helices approximately parallel to the principal axis of the diffusion tensor.

Three primary sources of NMR structural restraints were used in the structure determination: NOE-derived interproton distance restraints, backbone and side-chain torsion angle restraints, and orientational restraints in the form of backbone one-bond residual dipolar couplings. All assigned long range ($|i - j| > 5$) NOE-derived interproton distance restraints, both intra- and intersubunit, involve methyl groups and were derived from multidimensional NOE spectra recorded on samples in which at least one subunit was ^{15}N/^{13}C/^{2}H/(Val-Leu-Ile)-methyl-protonated. A summary of the structural statistics is provided in Table I, and a best fit superposition of the backbone atoms of the final ensemble of 100 simulated annealing structures is shown in Fig. 4*A*. Despite the fact that no attempt was made to assign the majority of non-methyl-based NOEs, the structures calculated from the experimental restraints are of high quality in terms of both coordinate precision and structure quality indicators (Table I). As such, the current approach therefore demonstrates the feasibility of obtaining high resolution NMR structures using predominantly methyl-based NOE-derived interproton distance restraints in conjunction with torsion angle and orientational dipolar coupling restraints. This approach should also be applicable to even larger systems where it becomes increasingly difficult to obtain high quality spectra on a uniformly ^{13}C,^{15}N-labeled sample due to even faster proton relaxation (61).

Overall Structure of IIA^{Chb*}—The solution structure of IIA^{Chb*} reveals that the three subunits of the homotrimer are arranged in a parallel fashion with the cross-section making an equilateral triangle (Fig. 5*A*, *right-hand panel*). Consistent with the 3-fold symmetry, the residual dipolar couplings measured for the backbone N-H, N-C′, and Cα-C′ vectors of the ordered residues fit to a fully axial symmetric alignment tensor, and the principal axis of alignment tensor coincides with the 3-fold symmetry axis of the trimer (62). Each subunit of the IIA^{Chb*} trimer comprises a three-helix bundle with an up-down topology in which helix 2 is antiparallel to helices 1 and 3. The three-helix bundle displays a small degree of left-handed supercoiling. Each helix has a span of nearly 30 residues (α1, residues 17–43; α2, residues 47–73; and α3, residues 85–113). The N-terminal 3 residues and C-terminal 2 residues are unstructured in solution (Fig. 4*B*) and are located on opposite sites of the protein. A tight turn (residues 44–46) connects helices 1 and 2, while an 11-residue flexible loop (residues 74–84), located in close proximity to the N terminus, bridges helices 2 and 3. These flexible/disordered regions are characterized by small heteronuclear ^{15}N-{^{1}H} NOE values (≤0.6) and low backbone coordinate precision (Fig. 4*B*). The functional and/or structural role of the flexible loop is unclear, but it is possible that its interaction with additional unstructured residues at the N terminus of wild-type IIA^{Chb} may be responsible for aggregation of the wild-type protein, rendering it unsuitable for structural studies.

Helix 3, which is arranged directly around the 3-fold symmetry axis, is primarily responsible for the assembly of the IIA^{Chb*} trimer via formation of a parallel coiled-coil structure (Fig. 5). Lining the trimer interface formed by helix 3 are a series of hydrophobic residues that include Leu-85, Val-88, Leu-92 (which is an Asp in wild-type IIA^{Chb}), Met-95, Leu-99, Leu-103, Leu-107, Leu-110, and Leu-114 (Fig. 5*A*). Inspection of the coiled-coil helices reveals the characteristic "knobs-into-holes" packing (63), in particular for the well defined Leu side chains, reminiscent of a leucine zipper structure (Fig. 5*C*). Unusual for a coiled-coil structure, the top view of the central helices reveals a slight right-handed twist (Fig. 5*A*, *right-hand panel*) (64, 65). Thus, to compensate for the lack of extensive left-handed supercoiling, the interacting hydrophobic residues do not strictly follow the alternating 4-3 heptad repeat of a canonical coiled-coil structure. About 25% of the total accessible surface area, 1917 Å^2 per subunit (total of 5751 Å^2) is buried at the trimer interface. Thus the IIA^{Chb*} trimer is expected to be very stable, and the structure is consistent with the observation that wild-type IIA^{Chb} behaves as a trimer at low (~140 nM) concentrations (Fig. 2*A*).

The interface between the adjacent subunits, A and C, C and B, and B and A, forms a deep depression on the surface of the molecule that is partially shielded from bulk solvent. The depressed surface comprises residues from helices 1 and 3 in one subunit (subunits A, B, or C) and from helices 2 and 3 in the other (subunits C, B, or A, respectively). Referenced with respect to helix 3, the N-terminal half of the crevice is formed by

TABLE I
Structural statistics

Experimental restraints	⟨SA⟩	$\langle\overline{\mathrm{SA}}\rangle_r$
r.m.s. deviations from experimental restraints[a]		
Distances (Å) (1290)	0.008 ± 0.002	0.010
Torsion angles (°) (729)	0.21 ± 0.05	0.41
^{13}Cα chemical shifts (ppm) (300)	1.12 ± 0.03	1.19
^{13}Cβ chemical shifts (ppm) (285)	0.64 ± 0.02	0.69
Residual dipolar coupling *R*-factors (%)[b]		
$^1D_{\mathrm{NH}}$ (252)	7.0 ± 0.1	7.1
$^1D_{\mathrm{NC'}}$ (255)	17.4 ± 0.9	15.2
$^2D_{\mathrm{C\alpha C'}}$ (249)	16.1 ± 1.0	17.7
Ramachandran map analysis[c]		
Percentage of residues in most favored region	93.5 ± 1.7	91.2
Percentage of residues in additionally allowed regions	5.7 ± 1.6	6.7
Number of bad contacts per 100 residues[c]	4.5 ± 1.6	7.4
Deviations from idealized covalent geometry		
Bonds (Å)	0.001 ± 0	0.004
Angles (°)	0.39 ± 0.02	0.59
Improper torsions (°)	0.58 ± 0.04	0.75
Coordinate precision (Å)[d]		
Backbone (N, Cα, C′)	0.37 ± 0.09	
All heavy atoms	0.84 ± 0.14	

[a] ⟨SA⟩ are the final 100 simulated annealing structures. $(\overline{\mathrm{SA}})_r$ is the restrained regularized mean structure derived from the mean coordinates obtained by averaging the coordinates of the 100 simulated annealing structures best fitted to each other (with respect to residues 13–73 and 83–114 of all three subunits simultaneously). The number of terms (on a trimer basis) for the various restraints is given in parentheses. None of the structures exhibits interproton distance violations >0.3 Å or torsion angle violations >5°. There are 828 interproton distance restraints comprising 246 sequential ($|i - j| = 1$), 258 medium range ($1 < |i - j| \leq 5$), and 90 long range ($|i - j| > 5$) intramolecular restraints and 234 intersubunit restraints. The intermolecular restraints are treated as ambiguous (*i.e.* no distinction can be made *a priori* for a NOE from subunit A to subunit B or C) by means of a $(\Sigma r^{-6})^{-1/6}$ sum representation. In addition, 462 distance restraints for 231 (77 per subunit) backbone hydrogen bonds within the three helices were also used. The torsion angle restraints comprise 255 ϕ, 255 ψ, and 219 side-chain χ restraints.

[b] The dipolar coupling *R*-factor, R_{dip}, which scales between 0 and 100%, is defined as the ratio of the r.m.s. deviation between observed and calculated values to the expected r.m.s. deviation if the vectors were randomly distributed, given by $[2D_a{}^2(4 + 3\eta^2)/5]^{1/2}$ where D_a is the magnitude of the principal component of the alignment tensor and η is the rhombicity (71). For a trimer the alignment tensor is always axially symmetric (η = 0). The value of D_a^{NH}, derived from the distribution of normalized dipolar couplings (74), is −12.1 Hz.

[c] Calculated with the program PROCHECK (75). The dihedral angle *G*-factors for the ensemble of simulated annealing structures are 0.64 ± 0.05, 0.86 ± 0.05, 0.54 ± 0.09, and 0.21 ± 0.14 for ϕ/ψ, χ_1/χ_2, χ_1, and χ_3/χ_4, respectively. The WHATIF first and second generation packing scores (76) for the restrained regularized mean structure are 2.10 and 3.52, respectively; values larger than −0.5 and 0, respectively, are considered to represent high quality structures.

[d] The precision of the coordinates is defined as the average atomic r.m.s. difference between the individual 100 simulated annealing structures and the corresponding mean coordinates obtained by best fitting residues 17–73 and 83–114 of all three subunits simultaneously. Residues 14–16, 74–82, and 115–116 are disordered in solution.

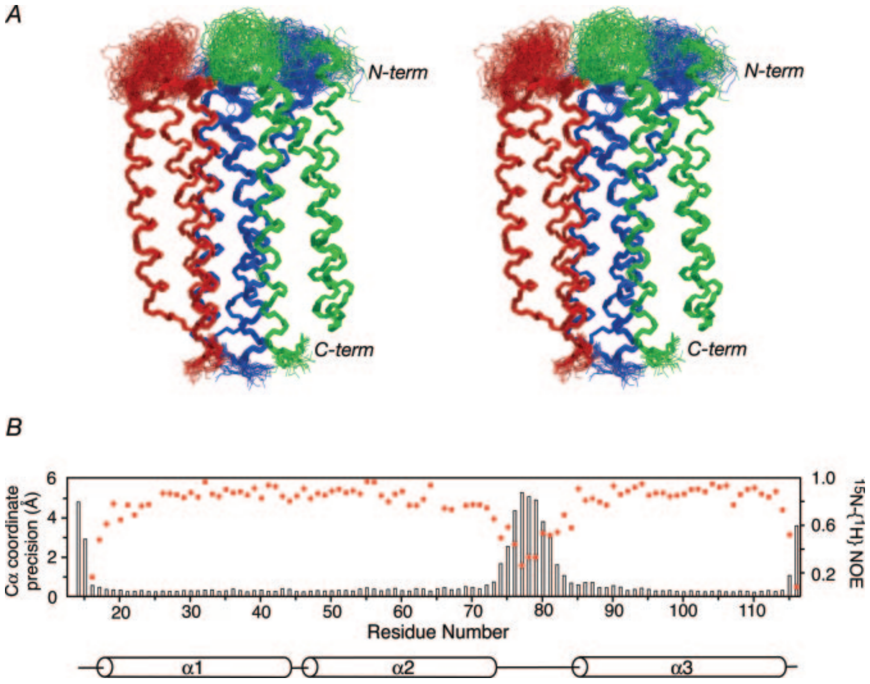

FIG. 4. **Structure of IIA$^{\mathbf{Chb*}}$.** *A*, stereoview of a best fit superposition of the backbone (N, Cα, and C′) atoms of the final 100 simulated annealing structure of the IIA$^{\mathrm{Chb*}}$ double mutant. The three subunits A, B, and C are colored in *red*, *blue*, and *green*, respectively. Best fitting was carried out with respect to the ordered residues, 17–63 and 83–114, of all three subunits. *B*, Cα coordinate precision and steady-state ^{15}N-{^{1}H} NOE represented by a *bar graph* and *red solid circles*, respectively, as a function of residue number. Precision is defined as the average atomic r.m.s. difference between the 100 individual simulated annealing structures and the mean coordinate positions. The secondary structure is delineated at the *bottom* of the figure.

hydrophobic and non-polar side chains, whereas several charged residues spot the C-terminal half of the depression (Fig. 6*A*). Since the buried surface between the adjacent subunits in a coiled-coil trimer is larger than that in a dimer, it has been noted that the corresponding sites are often enriched for hydrophobic residues (66). In fact, charged residues of opposite signs located at positions *e* and *g* of the heptad helical repeat are one of the determinants for coiled-coil dimer formation (67, 68). Thus, with charged residues located deep in the surface crevice, a possible stabilization mechanism for the IIA^{Chb} tri-

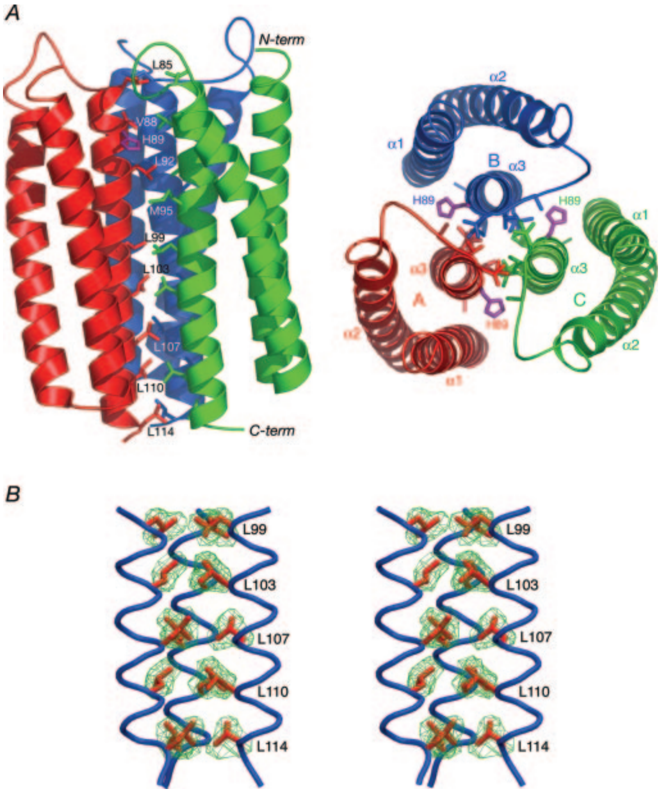

FIG. 5. **Topology of IIA^{Chb*} and details of the trimer interface.** *A*, ribbon diagram representation showing two views, parallel (*left panel*) and orthogonal (*right panel*) to the long axes of the helices with the three subunits, A, B, and C, colored in *red*, *blue*, and *green*, respectively. Hydrophobic side chains at the trimer interface are also shown as *bonds* in the respective color of the subunit. The active site histidine (His-89) is shown in *purple*. Note that the side-chain conformation for residue Met-95 is not well defined due to insufficient experimental restraints. The three α-helices are labeled in the *right-hand panel*. *B*, stereoview showing a close-up of the central helices (helix α3 from each subunit) at the trimer interface illustrating the leucine coiled-coil structure. The conformational space sampled by the leucine side chains (residues 99, 103, 107, 110, and 114) is represented by an isosurface of the reweighted atomic probability density map calculated from the final ensemble of 100 simulated annealing structures and drawn at a threshold of 20% (*green grid*). The backbone of residues 98–115 and the side-chain coordinates of the restrained regularized mean structure are shown as *blue tubes* and *red bonds*, respectively.

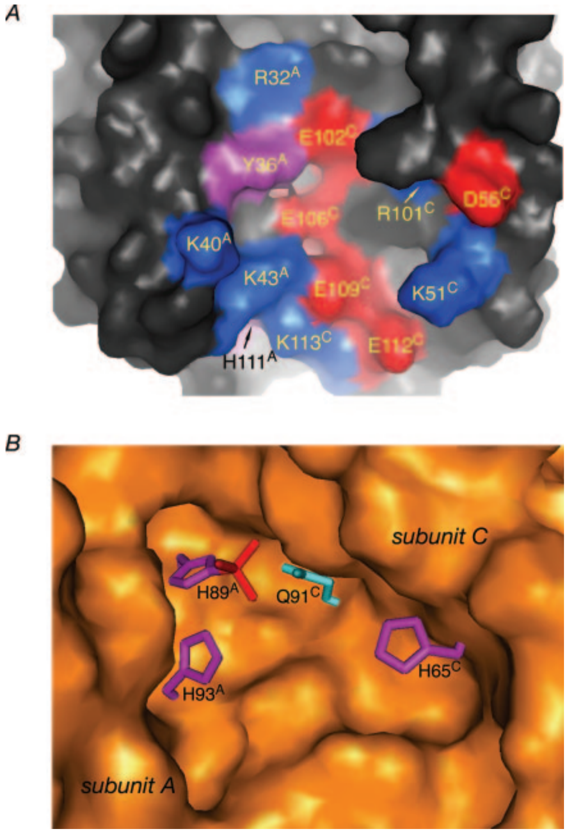

FIG. 6. **Surface representation of the depression between the two adjacent subunits of the IIA^{Chb*} trimer.** *A*, the *bottom half* of the depression (*i.e.* closest to the C terminus) features a network of electrostatic interactions. Positively and negatively charged side chains are colored in *blue* and *red*, respectively; tyrosine and histidine are colored in *purple*. *B*, structural model for phosphorylated IIA^{Chb*}. The phosphoryl group (shown in *red*) bonded to the Nε-2 of the active site histidine (His-89 of subunit A, shown in *purple*) was modeled in standard geometry. Neighboring residues in the crevice are also depicted: these include His-65 (colored in *purple*) and Gln-91 (shown in *cyan*) of subunit C and His-93 of subunit A (colored in *purple*). In *B*, the side chains of interest are represented by *bonds*, and the molecular surface etched behind the displayed side chains is colored in *orange*. In both panels the subunit of origin (subunit A or subunit C) is indicated in the residue labeling by a *superscript*.

mer would involve balancing of charges. Indeed pairs of counterions are formed between the following pairs of side-chains residues: Arg-32^{A} and Glu-102^{C}, Lys-43^{A} and Glu-106^{C}, Lys-43^{A} and Glu-109^{C}, Lys-51^{C} and Glu-112^{C}, Arg-101^{C} and Asp-55^{C}, and Lys-113^{C} and Glu-109^{C}. In contrast to the dimeric coiled-coil, the interacting charged residues are not restricted to the coiled-coil-forming helices (*i.e.* helix 3). Thus the attractive coulombic interactions between the partially buried charged residues actually further stabilize the IIA^{Chb*} trimer.

The Active Site—The active site histidine, His-89, is phosphorylated at the Nε-2 position by HPr (33). His-89 is located near the N terminus of helix 3, surrounded by predominantly hydrophobic residues. We modeled a phosphoryl group bonded to the Nε-2 atom of His-89 using idealized covalent geometry (Fig. 6*B*). It is worth noting that, due to steric hindrance, His-89 (irrespective of rotameric state about the χ_1 and χ_2 side-chain torsion angles) cannot be phosphorylated at the Nδ-1 position. Deep in the pocket, the negative charge of the phosphoryl group bonded to His-89^{A} is neutralized by (*a*) the positive dipole associated with the N terminus of helix 3; (*b*) a potential electrostatic interaction with the side chain of protonated His-93^{A} whose Nε-2 atom is on average ~4 Å away from the oxygen atoms of the phosphoryl group (Fig. 6*A*), reminiscent of the situation in IIA^{Glc} (69); and (*c*) a potential hydrogen bond between the phosphoryl group and the carboxyamide group of Gln-91^{C} of the adjacent subunit, which is less than 3 Å away (Fig. 6*B*). It has been speculated in the case of *L. lactis* IIA^{Lac} that His-65^{C} (in the current numbering scheme) is also involved in the stabilization of the phosphorylated state by forming a histidine triad (18). In the structure of IIA^{Chb*}, however, His-65^{C} is more than 8 Å away from the phosphoryl group of His-89^{A}. It is possible that an interaction between the side chains of His-65^{C} and Gln-91^{C} serves to optimally orient the side chain of Gln-91^{C} for hydrogen bonding with the phosphoryl group on His-89^{A}. In addition, sequence conservation of His-65 in *L. lactis* IIA^{Lac} and *E. coli* IIA^{Chb} (Fig. 1) may suggest that His-65 is possibly involved in protein-protein interactions with HPr and/or IIB^{Chb}. Thus, we suggest that partial sequestration of the phosphoryl group from bulk solvent coupled with electrostatic and/or hydrogen bonding interactions with the positive helix dipole and neighboring residues in the deep active site pocket are involved in stabilizing the phosphohistidine of IIA^{Chb}.

Comparison of the Structures of E. coli IIA^{Chb*} and L. lactis IIA^{Lac}—Both the crystal structure of *L. lactis* IIA^{Lac} (18) and

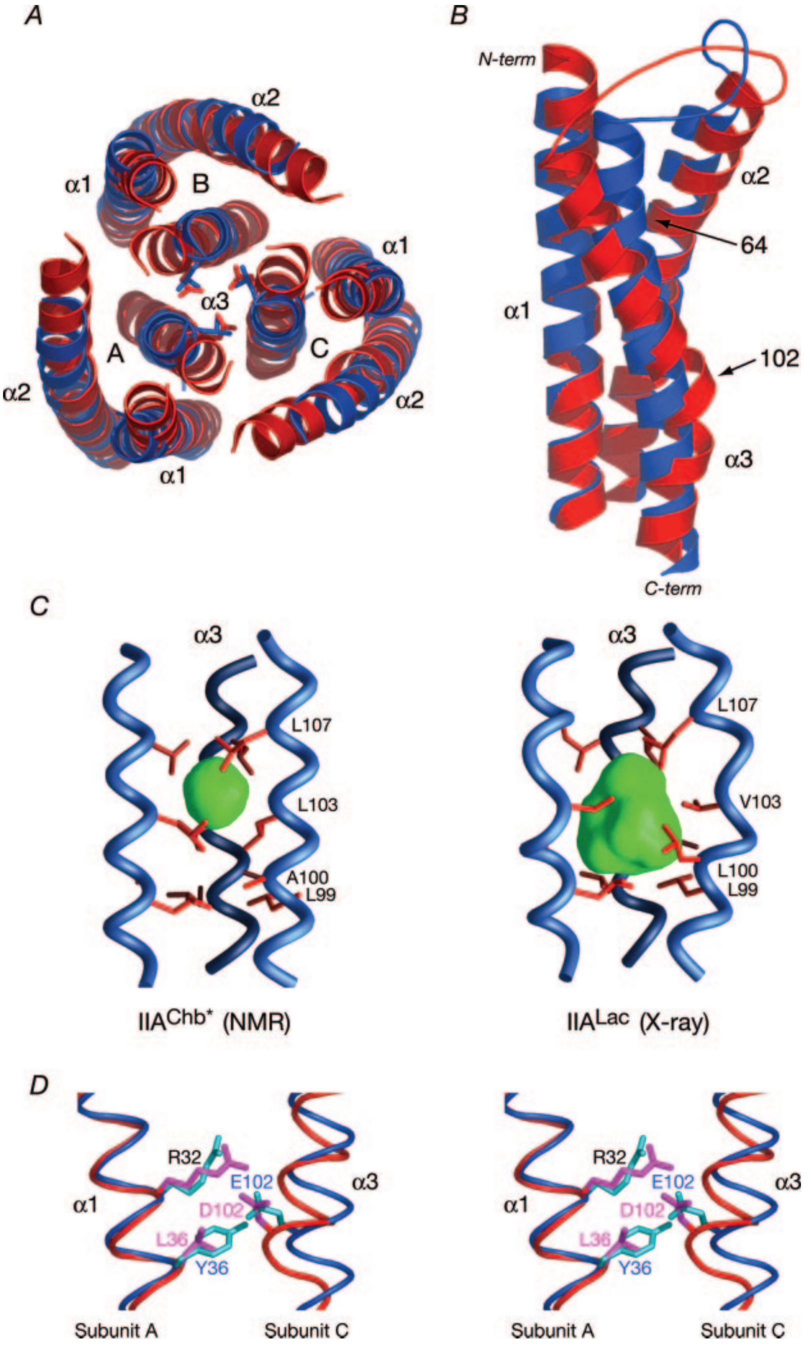

FIG. 7. **Comparison of the NMR structure of *E. coli* IIA^{Chb*} and the crystal structure of *L. lactis* IIA^{Lac}.** *A* and *B*, ribbon diagrams showing best fit superpositions of the restrained regularized mean structure of IIA^{Chb*} (*blue*) and *L. lactis* IIA^{Lac} (*red*). Two views, orthogonal and parallel to the long axes of the helices, are shown in *A* and *B*, respectively, with the trimer displayed in *A* and an individual subunit in *B*. Best fitting was carried out with respect to the backbone atoms of helices 1 (residues 17–43) and 2 (residues 47–73) of all three subunits in *A* and with respect to helix 1 (residues 17–43) and the N-terminal half of helix 2 (residues 47–63) in *B*. For clarity, only the helices are shown in *A*, and the disordered N- and C-terminal residues are omitted in *B*. The side chains of Leu-92 of IIA^{Chb*} and the equivalent Asp of IIA^{Lac} are represented as *bonds* in *A*, and their Cγ atom positions are 1.02, 0.92, and 0.92 Å apart for subunits A, B, and C, respectively. The three subunits are indicated in *A*, and the three helices of a single subunit are labeled in *B*. Note that the distance between the C-terminal end of helix 2 and the N-terminal end of helix 3 is significantly longer in IIA^{Lac} (~21 Å) than in IIA^{Chb} (~15 Å), yet the number of residues in the loop connecting helices 2 and 3 is 3 residues fewer in IIA^{Lac}. This may account for the observation that this loop is ordered in IIA^{Lac} but disordered in IIA^{Chb}. *C*, buried hydrophobic cavity (*green*) in IIA^{Chb*} (*left-hand panel*) and the crystal structure of *L. lactis* IIA^{Lac} (*right-hand panel*). The backbone atoms of residues 95–111 of the three subunits are depicted as tubes (*blue*), and the side chains of residues 99, 100, 103, and 107 are displayed in *red* as *bonds* (numbering scheme of IIA^{Chb*}). The cavity was calculated and displayed as a surface (*green*) using the program GRASP (32). The volume of the cavity in IIA^{Chb*} is 45 Å^3 and lined by the side chains of Leu-103 and Leu-107; the volume of the cavity of IIA^{Lac} is 230 Å^3 and lined by the side chains of Leu-99, Leu-100, Val-103, and Leu-107. *D*, comparison of the intersubunit interactions between helix 1 (subunit A) and helix 3 (subunit C) at the site of the kink in helix 3 (Glu-102) observed in the NMR structure of IIA^{Chb*} and the x-ray structure of IIA^{Lac}. The backbone (*blue* for IIA^{Chb*} and *red* for IIA^{Lac}) is displayed as a *tube*, and the side chains (*cyan* for IIA^{Chb*} and *purple* for IIA^{Lac}) are displayed as *bonds*. The coordinates for the crystal structure of *L. lactis* IIA^{Lac} are taken from Ref. 18 (Protein Data Bank code 1E2A).

the NMR structure of *E. coli* IIA^{Chb*} are trimeric with identical overall topologies. Thus, the trimeric nature of *E. coli* IIA^{Chb*} fulfills its sequence and functional homology to *L. lactis* IIA^{Lac}. Indeed the bottom half of the depressed surface between the adjacent A and C subunits of IIA^{Lac} is also spotted with charged residues. Comparison of the sequences of IIA^{Lac} and IIA^{Chb} (Fig. 1) reveals that the charged residues (Fig. 6*A*) are either conserved (Arg-32, Lys-40, and Glu-112), conservatively substituted (Arg-101 Lys, Glu-102 → Asp), or subject to simultaneous compensatory substitutions involving ion pairs (Lys-43 → Glu and Glu-106 → His pair, and Lys-51 → Asp and Glu-112 → Lys pair). Thus, the total net charge in the surface crevice is always kept close to zero, thereby eliminating repulsive and desolvation effects that could potentially destabilize the trimer.

There are some small differences in the extent of the helices between the two structures: helix 1 has 3 additional residues at its N terminus, helix 2 has 3 additional residues at its C terminus, and helix 3 is 2 residues shorter at its C terminus in IIA^{Lac} relative to IIA^{Chb*}. The shorter loop connecting helices 2 and 3 in IIA^{Lac} relative to IIA^{Chb*} (8 *versus* 11 residues) coupled with the longer distance between the C terminus of helix 2 and the N terminus of helix 3 in IIA^{Lac} relative to IIA^{Chb} (~21 *versus* ~15 Å) and the additional presence of a proline residue in the IIA^{Lac} loop may account for the observation that this loop is ordered in the crystal structure of IIA^{Lac} with *B*-factors less than 40 Å^2, whereas it is highly disordered for IIA^{Chb*} in solution (see Fig. 4).

Excluding the disordered regions (residues 14–16, 74–84, and 115–116), the backbone atomic r.m.s. difference between the crystal structure of IIA^{Lac} and the NMR structure of

TABLE II

Structural comparison of the helices of the NMR structure of IIA^{Chb*} and the crystal structure of IIA^{Lac}

Helix[a]	N-H dipolar coupling R-factor, $R_{\mathrm{dip}}^{\mathrm{NH}}$ [b]		Backbone r.m.s. difference
	IIA^{Lac} (x-ray)	IIA^{Chb*} (NMR)[c]	
	%		Å
$\alpha 1 + \alpha 2 + \alpha 3$	37.5	7.3	1.95
$\alpha 1 + \alpha 2^{N}$	20.1	7.5	1.17
$\alpha 1 + \alpha 2$	24.0	6.9	1.54
$\alpha 2 + \alpha 3$	43.2	7.2	2.15
$\alpha 1 + \alpha 3$	42.0	7.8	2.03
$\alpha 1$	22.4	7.5	1.41
$\alpha 2$	25.4	6.2	1.63
$\alpha 2^{N}$	15.5	7.4	0.52
$\alpha 2^{C}$	35.9	2.7	1.56
$\alpha 3$	54.5	8.1	2.30
$\alpha 3^{N}$	47.5	9.3	2.46
$\alpha 3^{C}$	50.3	6.2	1.29

[a] Helices $\alpha 1$, $\alpha 2$, and $\alpha 3$ comprise residues 17–43, 47–73, and 85–113, respectively. The crystal structure of IIA^{Lac} displays a bend (~27°) and kink (~40°) in helices 2 (centered around residues 64 and 65) and 3 (centered around residues 102 and 103), respectively: the N-terminal halves of helices 2 ($\alpha 2^{N}$) and 3 ($\alpha 3^{N}$) comprise residues 47–63 and 85–101, respectively; the C-terminal halves of helices 2 ($\alpha 2^{C}$) and 3 ($\alpha 3^{C}$) comprise residues 66–73 and 104–113, respectively. The $R_{\mathrm{dip}}^{\mathrm{NH}}$ values for helix 2 exclude residues 66 and 67 of subunit B and residue 65 of subunit C, which yield anomalously high fitting errors to the IIA^{Lac} crystal structure; if all the N-H dipolar couplings of helix 2 are fitted to the IIA^{Lac} crystal structure, $R_{\mathrm{dip}}^{\mathrm{NH}}$ is increased to 37.1%. The backbone atomic (N, Cα, and C′) r.m.s. differences relate to the restrained regularized mean NMR structure of IIA^{Chb*} and the crystal structure (Protein Data Bank code 1E2A) of IIA^{Lac}.

[b] The definition of the dipolar coupling R-factor is given in Footnote b in Table I.

[c] Restrained regularized mean structure.

IIA^{Chb*} is 1.94 Å for the trimer (Fig. 7*A*) and 1.71 ± 0.04 Å for the individual subunits (Fig. 7*B*). These differences are substantial and outside the coordinate errors of the two structures. A large contribution to the atomic r.m.s. difference originates from helix 3 (Fig. 7*B*). Thus, the backbone atomic r.m.s. difference between the two structures for residues 17–73 (helices 1 and 2 and the turn connecting them) is reduced to 1.06 ± 0.16 Å per subunit. From the perspective of the trimer interface, it is worth noting that when helices 1 and 2 of all three subunits are superimposed, the Cγ atom of Leu-92 in IIA^{Chb*} (mutated from an Asp in the wild-type protein) is less than 1 Å from the Cγ atom of the corresponding Asp of IIA^{Lac} (Fig. 7*A*). This clearly supports the hypothesis that the buried Asp-79 in wild-type IIA^{Chb} stabilizes the trimer by coordinating a divalent cation in the same fashion as in IIA^{Chb} and further demonstrates that the Asp to Leu point mutation has minimal impact on the structure. Note that the equivalent mutation in *L. lactis* IIA^{Lac} does not result in any significant structural perturbation in the crystal structure (Protein Data Bank code 2E2A) relative to that of the wild-type (Protein Data Bank code 1E2A; Ref. 18) with a Cα atomic r.m.s. difference of only 0.87 Å (0.66 Å for the helices) between the two sets of coordinates.

In the crystal structure of *L. lactis* IIA^{Lac}, helix 3 exhibits a large 40° kink centered around residues 102 and 103 (Figs. 7*B* and *C*). This results in the presence of a very large (230-Å^3), completely buried cavity in the crystal structure (Fig. 7*C*, *right-hand panel*) in which the heavy atom derivative, trimethyl lead acetate, is located (18). The cavity in IIA^{Lac} is entirely hydrophobic and lined by the side chains of Leu-99, Leu-100, Val-103, and Leu-107 (using the current numbering scheme, Fig. 1). In contrast, the NMR structure of IIA^{Chb*} exhibits only a 7° bend at the same location, and the volume of the corresponding cavity is reduced to 45 Å^3 (Fig. 7*C*, *left-hand panel*). This smaller cavity in IIA^{Chb*} is also entirely hydrophobic and lined by the side chains of Leu-103 and Leu-107. The differences related to cavity size and the kinking of helix 3 are associated with concomitant structural differences in helix 2, which exhibits a bend of 27° centered around residues 64 and 65 in IIA^{Lac} compared with only 18° in IIA^{Chb*} (Fig. 7*B*).

The question immediately arises as to whether these differences are real and can be readily discerned from the NMR data. NOE-derived interproton distance restraints are limited to distances less than 5–6 Å and hence cannot distinguish a bent from a straight helix. Dipolar couplings, however, provide very sensitive long range information in the form of orientation of atomic vectors relative to the alignment tensor that can be used to quantitatively ascertain structural differences between the solution and crystal states. In this case, since the alignment tensor is axially symmetric, the orientational information is restricted to the angle between atomic vectors and the principal axis of the alignment tensor, which coincides with the 3-fold symmetry axis of the trimer. The crystal structure of IIA^{Lac} was solved at 2.3-Å resolution, and one would therefore expect a dipolar coupling R-factor, $R_{\mathrm{dip}}^{\mathrm{NH}}$ (70), of around 15–20% for the N-H backbone dipolar couplings (24, 25, 71, 72). The overall $R_{\mathrm{dip}}^{\mathrm{NH}}$ factor for all the three helices of the IIA^{Lac} trimer is 38% compared with 22% for helix 1, 25% for helix 2, and 55% for helix 3 (Table II). One can therefore conclude that whereas the path and orientation of helix 1 in the IIA^{Lac} and IIA^{Chb*} trimers are essentially the same, the difference in kink angle for helix 3 is real. With respect to helix 2 of IIA^{Lac}, the $R_{\mathrm{dip}}^{\mathrm{NH}}$ factor for the N-terminal half ($\alpha 2^{N}$, residues 47–63) is 16% compared with 36% for the C-terminal half ($\alpha 2^{C}$, residues 66–73), which clearly indicates that the difference in bend angle for helix 2 in IIA^{Chb*} and IIA^{Lac} results in a different orientation of the C-terminal half of helix 2 between the two proteins. This is reflected in the much smaller backbone atomic r.m.s. difference between IIA^{Chb*} and IIA^{Lac} for helices $\alpha 1$ plus $\alpha 2^{N}$ (1.17 Å for the trimer) than for helices $\alpha 1$ plus $\alpha 2^{C}$ (1.72 Å for the trimer).

A comparison of the intersubunit interactions involving residue 102 of helix 3, the site of the 40° kink in IIA^{Lac}, reveals a probable source of the principal structural differences between IIA^{Chb*} and IIA^{Lac} (Fig. 7*D*). In IIA^{Chb*}, Glu-102 of subunit C forms a potential salt bridge with Arg-32 and a hydrogen bond with the hydroxyl group of Tyr-36 located in helix 1 of subunit A. All three side chains are partially buried and located in the deep surface crevice at the intersubunit interface formed by helices 1 and 3 (Fig. 6*A*). Moreover the guanidino group of Arg-32 is directed toward the protein interior, and neutralization of its positive charge is probably important for structural integrity. Glu-102 and Tyr-36 are substituted in IIA^{Lac} by two shorter side chains, aspartate and leucine. The location of the carboxylate group of Asp-102 of IIA^{Lac} (current numbering scheme) is essentially identical to that of Glu-102 of IIA^{Chb*} so that the salt bridge with Arg-32 is preserved, and the methyl groups of Leu-36 pack against the β-methylene group of Asp-

102. Because the side chains of aspartate and leucine are ~1.5 and 3.5 Å shorter, respectively, than those of glutamate and tyrosine, a compensatory displacement of the backbone of helix 3, in the form of a kink centered at residue 102, occurs (Fig. 7*D*), thereby creating a large internal hydrophobic cavity at the trimer interface of IIA^{Lac} formed by helix 3 from the three subunits (Fig. 7*C*). Presumably the interactions involving Asp-102, Arg-32, and Leu-36 in IIA^{Lac} coupled with the need to neutralize the partially buried positive charge associated with the guanidino group of Arg-32 compensate for any energetic loss that may accompany the creation of the cavity.

Concluding Remarks—We have determined the solution structure of a double mutant of IIA^{Chb} from the *N,N′*-diacetylchitobiose branch of the *E. coli* PTS signal transduction pathway. Wild-type IIA^{Chb} is composed of a mixture of aggregates ranging in size from a trimer to high order oligomers, thereby precluding its structural characterization. Using rational mutagenesis on the basis of the crystal structure of the homologous enzyme IIA^{Lac} from *L. lactis*, we constructed a double mutant IIA^{Chb}-NΔ13/D92L (IIA$^{\text{Chb}*}$) that forms a well behaved homogeneous, monodisperse trimer. As the three symmetrically related active sites of IIA^{Chb} are located at the interface of two adjacent subunits (A and C, C and B, and B and A), the recognition surface for the upstream (HPr) and downstream (IIB^{Chb}) interaction partners would be significantly different from that in the previously proposed dimer of IIA^{Chb} (34). Thus, although it has been noted that mutation of just a few residues can switch the oligomerization state of a coiled-coil protein between dimeric and trimeric forms (73), the quaternary structure of *E. coli* IIA^{Chb} is preserved despite sequence differences with respect to *L. lactis* IIA^{Lac} (Fig. 1). In this sense, the functional role of enzyme IIA^{Chb} as a member of the lactose/chitobiose branch of the PTS, that is its interactions with other components of this signaling network, goes hand in hand with structural conservation of a trimeric oligomerization state. Finally the present NMR structure of IIA$^{\text{Chb}*}$ sets the stage for future NMR structural studies of the 65–70-kDa IIA$^{\text{Chb}*}$-HPr and IIA$^{\text{Chb}*}$-IIB^{Chb} complexes for which the methyl-based NOE approach combined with backbone dipolar couplings used in this study is likely to find considerable utility.

Acknowledgments—We thank Drs. Junji Iwahara and Mengli Cai for helpful discussions, Dr. In-Ja Byeon for assistance with light-scattering measurements, Drs. Dan Garrett and Frank Delaglio for software and technical support, and Dr. Saul Roseman for the gift of the wild-type IIA^{Chb} plasmid. This study utilized the high performance computational capabilities of the Biowulf PC/Linux cluster at the National Institutes of Health, Bethesda, MD (biowulf.nih.gov).

REFERENCES

1. Kundig, W., Ghosh, S., and Roseman, S. (1964) *Proc. Natl. Acad. Sci. U. S. A.* **52,** 1067–1074
2. Postma, P. W., Lengeler, J. W., and Jacobson, G. R. (1993) *Microbiol. Rev.* **57,** 543–594
3. Robillard, G. T., and Broos, J. (1999) *Biochim. Biophys. Acta* **1422,** 73–104
4. Siebold, C., Flükiger, K., Beutler, R., and Erni, B. (2001) *FEBS Lett.* **504,** 104–111
5. Wittekind, M., Rajgopal, P., Cranchini, B. R., Reizer, J., Saier, M. H., and Klevit, R. E. (1992) *Protein Sci.* **1,** 1363–1376
6. Kalbitzer, H. R., and Hengstenberg, W. (1993) *Eur. J. Biochem.* **216,** 205–214
7. van Nuland, N. A. J., Hangyi, I. W., van Shaik, R. C., Berendsen, H. J. C., van Gunsteren, W. F., Scheek, R. M., and Robillard, G. T. (1994) *J. Mol. Biol.* **237,** 544–559
8. Ab, E., Schuurman-Wolters, G. K., Reizer, J., Saier, M. H., Dijkstra, M., Scheek, R. M., and Robillard, G. T. (1997) *Protein Sci.* **6,** 304–314
9. Ab, E., Shuurman-Walters, G. K., Nijlant, D., Dijkstra, K., Saier, M. H., Robillard, G. T., and Scheek, R. M. (2001) *J. Mol. Biol.* **308,** 993–1009
10. Garrett, D. S., Seok, Y.-J., Liao, D.-I., Peterkofsky, A., Gronenborn, A. M., and Clore, G. M. (1997) *Biochemistry* **36,** 2517–2530
11. Legler, P. M., Cai, M., Peterkofsky, A., and Clore, G. M. (2004) *J. Biol. Chem.* **279,** 39115–39121
12. Liao, D.-I., Kapadia, G., Reddy, P., Saier, M. H., Reizer, J., and Herzberg, O. (1991) *Biochemistry* **30,** 9538–9594
13. Worthylake, D., Meadow, N. D., Roseman, S., Liao, D.-I., Herzberg, O., and Remington, S. J. (1991) *Proc. Natl. Acad. Sci. U. S. A.* **88,** 10383–10386
14. Herzberg, O., Reddy, P., Sutrina, S., Saier, M. H., Reizer, J., and Kapadia, G. (1992) *Proc. Natl. Acad. Sci. U. S. A.* **89,** 2499–2503
15. Jia, Z., Quail, J. W., Waygood, E. B., and Delbaere, L. T. (1993) *J. Biol. Chem.* **268,** 22490–22501
16. Liao, D.-I., Silverton, E., Seok, Y.-J., Lee, B. R., Peterkofsky, A., and Davies, D. R. (1996) *Structure* **4,** 861–872
17. Nunn, R. S., Markovic-Housley, Z., Genovesio-Taverne, G., Flükiger, K., Rizkallah, P. J., Jansonius, J. N., Schirmer, T., and Erni, B. (1996) *J. Mol. Biol.* **259,** 502–511
18. Sliz, P., Engelmann, R., Hengstenberg, W., and Pai, E. F. (1997) *Structure* (*Lond.*) **5,** 775–788
19. Van Montfort, R. L., Pijning, T., Kalk, K. H., Reizer, J., Saier, M. J., Thunnissen, M. M., Robillard, G. T., and Dijkstra, B. W. (1997) *Structure* (*Lond.*) **5,** 217–225
20. Van Montfort, R. L., Pijning, T., Kalk, K. H., Hangyi, I. W., Kouwijzer, M. L. C. E., Robillard, G. T., and Dijkstra, B. W. (1998) *Structure* (*Lond.*) **6,** 377–388
21. Schauder, S., Nunn, R. S., Lanz, R., Erni, B., and Schirmer, T. (1998) *J. Mol. Biol.* **276,** 591–602
22. Orniss, G. L., Erni, B., and Schirmer, T. (2003) *J. Mol. Biol.* **327,** 1111–1119
23. Garrett, D. S., Seok, Y.-J., Peterkofsky, A., Gronenborn, A. M., and Clore, G. M. (1999) *Nat. Struct. Biol.* **6,** 166–173
24. Wang, G., Louis, J. M., Sondej, M., Seok, Y.-J., Peterkofsky, A., and Clore, G. M. (2000) *EMBO J.* **19,** 5635–5649
25. Cornilescu, G., Lee, B. R., Cornilescu, C., Wang, G., Peterkofsky, A., and Clore, G. M. (2002) *J. Biol. Chem.* **277,** 42289–42298
26. Cai, M., Williams, D. C., Wang, G., Lee, B. R., Peterkofsky, A., and Clore, G. M. (2003) *J. Biol. Chem.* **278,** 25191–25206
27. Keyhani, N. O., and Roseman, S. (1997) *Proc. Natl. Acad. Sci. U. S. A.* **94,** 14367–14371
28. Zhang, M., Van Etten, R. L., and Stauffacher, C. V. (1994) *Biochemistry* **33,** 11097–11105
29. Su, X.-D., Taddei, N., Stefani, M., Ramponi, G., and Nordlund, P. (1994) *Nature* **370,** 575–578
30. Hays, J. B., Simoni, R. D., and Roseman, S. (1973) *J. Biol. Chem.* **248,** 941–956
31. de Vos, W. M., Boerrigter, I., van Rooyen, R. J., Reiche B., and Hengstenberg, W. (1990) *J. Biol. Chem.* **265,** 22554–22560
32. Nicholls, A., Sharp, K. A., and Honig, B. (1991) *Proteins* **17,** 297–309
33. Keyhani, N. O., Boudker, O., and Roseman, S. (2000) *J. Biol. Chem.* **275,** 33091–33101
34. Keyhani, N. O., Rodgers, M. E., Demeler, B., Hansen, J. C., and Roseman, S. (2000) *J. Biol. Chem.* **275,** 33110–33115
35. Goto, N. K., Gardner, K. H., Mueller, G. A., Willis, R. C., and Kay, L. E. (1999) *J. Biomol. NMR* **13,** 369–374
36. Garcia de la Torre, J., Huertas, M. L., and Carrasco, B. (2000) *Biophys. J.* **78,** 719–730
37. Delaglio, F., Grzesiek, S., Vuister, G. W., Zhu, G., Pfiefer, J., and Bax, A. (1995) *J. Biomol. NMR* **6,** 277–293
38. Garrett, D. S., Powers, R., Gronenborn, A. M., and Clore, G. M. (1991) *J. Magn. Reson.* **95,** 214–220
39. Clore, G. M., and Gronenborn, A. M. (1991) *Science* **252,** 1390–1399
40. Bax, A., and Grzesiek, S. (1993) *Acc. Chem. Res.* **26,** 131–138
41. Yang, D. W., and Kay, L. E. (1999) *J. Biomol. NMR* **14,** 273–276
42. Clore, G. M., and Gronenborn, A. M. (1998) *Trends Biotechnol.* **16,** 22–34
43. Cornilescu, G., Delaglio, F., and Bax, A. (1999) *J. Biomol. NMR* **13,** 289–302
44. Bax, A., Vuister, G. W., Grzesiek, S., Delaglio, F., Wang, A. C., Tschudin, R., and Zhu, G. (1994) *Methods Enzymol.* **239,** 79–105
45. Clore, G. M., Starich, M. R., and Gronneborn, A. M. (1998) *J. Am. Chem. Soc.* **120,** 10571–10572
46. Hansen, M. R., Hanson, P., and Pardi, A. (2000) *Methods Enzymol.* **317,** 220–240
47. Yang, D., Venters, R. A., Mueller, G. A., Choy, W. Y., and Kay, L. E. (1999) *J. Biomol. NMR* **14,** 333–343
48. Jaroniec, C. P., Ulmer, T. S., and Bax, A. (2004) *J. Biomol. NMR* **30,** 181–194
49. Nilges, M., Gronenborn, A. M., Brünger, A. T., and Clore, G. M. (1988) *Protein Eng.* **2,** 27–38
50. Garrett, D. S., Kuszewski, J., Hancock, T. J., Lodi, P. J., Vuister, G. W., Gronenborn, A. M., and Clore, G. M. (1994) *J. Magn. Reson. B* **104,** 99–103
51. Kuszewski, J., Qin, J., Gronenborn, A. M., and Clore, G. M. (1995) *J. Magn. Reson. B* **106,** 92–96
52. Clore, G. M., Gronenborn, A. M., and Tjandra, N. (1988) *J. Magn. Reson.* **131,** 159–162
53. Schwieters, C. D., and Clore, G. M. (2001) *J. Magn. Reson.* **152,** 288–302
54. Schwieters, C. D., Kuszewski, J., Tjandra, N., and Clore, G. M. (2003) *J. Magn. Reson.* **160,** 65–73
55. Clore, G. M., and Kuszewski, J. (2002) *J. Am. Chem. Soc.* **124,** 2866–2867
56. Grishaev, A., and Bax, A. (2004) *J. Am. Chem. Soc.* **126,** 7281–7292
57. Kuszewski, J., Gronenborn, A. M., and Clore, G. M. (1999) *J. Am. Chem. Soc.* **121,** 2337–2338
58. Schwieters, C. D., and Clore, G. M. (2001) *J. Magn. Reson.* **149,** 239–244
59. DeLano, W. L. (2002) *The PyMOL Molecular Graphics System*, DeLano Scientific, San Carlos, CA
60. Schwieters, C. D., and Clore, G. M. (2002) *J. Biomol. NMR* **23,** 221–225
61. Tugarinov, V., and Kay, L. E. (2004) *J. Am. Chem. Soc.* **126,** 9827–9836
62. Al-Hashimi, H. M., Bolton, P. J., and Prestegard, J. H. (2000) *J. Magn. Reson.* **142,** 153–158
63. Chothia, C. (1984) *Annu. Rev. Biochem.* **53,** 537–572
64. Lupas, A. (1996) *Trends Biochem. Sci.* **21,** 375–382
65. Harbury, P. B., Plecs, J. J., Tidor, B., Alber, T., and Kim, P. S. (1998) *Science* **282,** 1462–1467
66. Woolfson, D. N., and Alber, T. (1995) *Protein Sci.* **4,** 1596–1607
67. Zeng, X., Zhu, H., Lashuel, H., and Hu, J. C. (1997) *Protein Sci.* **6,** 2218–2226
68. McClain, D. L., Binfet, J. P., and Oakley, M. G. (2001) *J. Mol. Biol.* **313,**

373–383
69. Pelton, J. G., Torchia, D. A., Meadow, N. D., and Roseman, S. (1993) *Protein Sci.* **2,** 543–558
70. Clore, G. M., and Garrett, D. S. (1999) *J. Am. Chem. Soc.* **121,** 9008–9012
71. Bax, A., Kontaxis, G., and Tjandra, N. (2001) *Methods Enzymol.* **339,** 127–174
72. Williams, D. C., Cai, M., and Clore, G. M. (2004) *J. Biol. Chem.* **279,** 1449–1457
73. Harbury, P. B., Zhang, T., Kim, P. S., and Alber, T. (1993) *Science* **262,** 1401–1407
74. Clore, G. M., Gronenborn, A. M., and Bax, A. (1998) *J. Magn. Reson.* **133,** 216–221
75. Laskowski, R. A., MacArthur, M. W., Moss, D. S., and Thornton, J. M. (1993) *J. Appl. Crystallogr.* **26,** 283–291
76. Vriend, G., and Sander, C. (1993) *J. Appl. Crystallogr.* **26,** 47–60